

Pro+: Automated protrusion and critical shear stress estimates from 3D point clouds of gravel beds

Elowyn M. Yager¹  | Jaeho Shim¹ | Rebecca Hodge²  | Angel Monsalve¹ |
 Daniele Tonina¹  | Joel P. L. Johnson³ | Luke Telfer¹

¹Center for Ecohydraulics Research,
 Department of Civil and Environmental
 Engineering, University of Idaho, Moscow,
 Idaho, USA

²Department of Geography, Durham
 University, Durham, UK

³Department of Geological Sciences,
 University of Texas at Austin, Austin, Texas,
 USA

Correspondence

Elowyn M. Yager, Center for Ecohydraulics
 Research, Department of Civil and
 Environmental Engineering, University of
 Idaho, Moscow, Idaho, USA.
 Email: eyager@uidaho.edu

Funding information

Division of Earth Sciences; National Science
 Foundation, Grant/Award Number:
 EAR1921790

Abstract

The dimensionless critical shear stress (τ^*_c) needed for the onset of sediment motion is important for a range of studies from river restoration projects to landscape evolution calculations. Many studies simply assume a τ^*_c value within the large range of scatter observed in gravel-bedded rivers because direct field estimates are difficult to obtain. Informed choices of reach-scale τ^*_c values could instead be obtained from force balance calculations that include particle-scale bed structure and flow conditions. Particle-scale bed structure is also difficult to measure, precluding wide adoption of such force-balance τ^*_c values. Recent studies have demonstrated that bed grain size distributions (GSD) can be determined from detailed point clouds (e.g. using G3Point open-source software). We build on these point cloud methods to introduce Pro+, software that estimates particle-scale protrusion distributions and τ^*_c for each grain size and for the entire bed using a force-balance model. We validated G3Point and Pro+ using two laboratory flume experiments with different grain size distributions and bed topographies. Commonly used definitions of protrusion may not produce representative τ^*_c distributions, and Pro+ includes new protrusion definitions to better include flow and bed structure influences on particle mobility. The combined G3Point/Pro+ provided accurate grain size, protrusion and τ^*_c distributions with simple GSD calibration. The largest source of error in protrusion and τ^*_c distributions were from incorrect grain boundaries and grain locations in G3Point, and calibration of grain software beyond comparing GSD is likely needed. Pro+ can be coupled with grain identifying software and relatively easily obtainable data to provide informed estimates of τ^*_c . These could replace arbitrary choices of τ^*_c and potentially improve channel stability and sediment transport estimates.

KEY WORDS

critical shear stress, grain size, point cloud, protrusion, sediment transport

1 | INTRODUCTION

Sediment transport can influence channel stability, flooding risks, reservoir lifetimes, and aquatic habitat for threatened and endangered species (Duffin et al., 2023; Garcia, 2008). Bedload transport calculations typically include sediment motion thresholds that must be exceeded before transport begins. The dimensionless critical shear stress (critical Shields stress, τ^*_c) is a commonly used threshold, and the critical Shields stress for the median grain size (τ^*_{c50}) may be approximately uniform in lower-gradient gravel-bedded

rivers that experience hydraulically rough flow (Buffington & Montgomery, 1997; Shields, 1936). Despite this constant average value, substantial scatter exists between different gravel-bed rivers in both τ^*_{c50} (e.g. 0.01–0.1) and the critical Shields stress (τ^*_{ci}) for a given grain size on the bed (D_i). Recent studies show that τ^*_{c50} can also temporally vary within a river, further complicating the choice of a representative value (Charru et al., 2004; Haynes & Pender, 2007; Johnson, 2016; Masteller et al., 2019; Ockelford et al., 2019; Pretzlav et al., 2020; Rickenmann, 2020; Turowski et al., 2011). No generally applicable method exists to select a

specific τ^*_{c50} value in space and time within the scatter of observed values.

Variations in τ^*_c are attributed to methodological (# 1–2) and physical differences (# 3–5) in (1) onset of motion definitions, (2) sediment transport measurement techniques, (3) bed grain size distributions (GSD) including armouring, (4) flow characteristics (e.g. velocity profiles) and (5) bed structure (Bathurst, 2013; Buffington et al., 1992; Buffington & Montgomery, 1997; Hodge et al., 2013; Lamb et al., 2008, 2017a; Ockelford & Haynes, 2013; Recking, 2009; Schmeeckle et al., 2007; Shvidchenko et al., 2001; Voepel et al., 2019; Wiberg & Smith, 1987; Yager et al., 2012; Yager, Schmeeckle, & Badoux, 2018). Temporal variations in τ^*_c are not a methodological artefact because the same definition and method of estimating the onset of motion are usually employed in an individual channel/experiment over time. Consequently, the last three physical differences are the most mechanistically important to consider for both spatial and temporal variations in τ^*_c . Observed temporal variations in τ^*_c without significant bed GSD alterations further imply that near-bed flow hydraulic or bed structural changes alone could be responsible in some streams (Masteller et al., 2019). In theory, bed structure could also adjust faster than bed GSD in response to changes in flow or sediment supply over time.

Protrusion and intergranular friction are key components of bed structure that influence τ^*_c (Bi et al., 2011; Cúñez et al., 2022; Fenton & Abbott, 1977; Hodge et al., 2020; Luo et al., 2023; Masteller & Finnegan, 2017; Yager, Schmeeckle, & Badoux, 2018). Intergranular friction can empirically include the effects of particle imbrication, orientation, angularity, cohesion, interlocking, clustering and porosity. Protrusion, which is often defined as the distance a particle extends above the surrounding mean bed elevation, varies with relative particle size (Hodge et al., 2020; Kirchner et al., 1990; Smith et al., 2023). Protrusion exerts strong controls on the applied fluid forces on a particle by altering the grain area exposed to the flow as well as the pressure distribution around the grain (Schmeeckle et al., 2007). Particles with greater protrusion typically have higher drag forces but possibly lower lift forces (Schmeeckle et al., 2007). Conversely, resisting forces impeding motion decline as particle protrusion increases because higher protruding particles are less buried by surrounding sediment (Sanguinito & Johnson, 2012; Yager, Schmeeckle, & Badoux, 2018). The net result of these driving and resisting forces is that higher protrusion lowers τ^*_c to make particles easier to move. In theory, τ^*_c can decrease by orders of magnitude as particle protrusion changes from a completely buried grain to one that is fully exposed (Hodge et al., 2020; Yager, Schmeeckle, & Badoux, 2018).

Despite its importance, protrusion is not widely used to estimate τ^*_c because of two major limitations. First, protrusion needs to be combined with validated force balance models to estimate τ^*_c , which could be addressed by testing published force balance models but few suitable datasets exist (Kirchner et al., 1990; Lamb et al., 2008; Voepel et al., 2019; Wiberg & Smith, 1987; Yager, Schmeeckle, & Badoux, 2018). Second, protrusion is not easily measured in the field or laboratory flume. It is often manually measured using a ruler or point gauge, which is subject to potentially large errors and subjective measurement location choices (Kirchner et al., 1990; Yager, Schmeeckle, & Badoux, 2018). Any manual measurement of protrusion is also extremely time consuming and could disturb the bed.

Protrusion has been estimated from high-resolution point clouds or 3D bed topographies (Hodge et al., 2020), which removes some measurement uncertainties and has lower bed disturbance potential. But such measurements still require identification of grain boundaries, which is often carried out manually (Hodge et al., 2013).

In addition to these limitations, the protrusion definition that, when used in force balance equations, provides the most representative τ^*_c value is also uncertain. Protrusion is often divided into exposure and projection, which are defined as the distances a grain extends above a locally high bed elevation and the local surrounding mean bed elevation, respectively (Buffington et al., 1992; Kirchner et al., 1990). In theory, exposure accounts for particle sheltering from the flow by upstream obstructions whereas projection incorporates the effects of a velocity profile on particle motion. The locations included in the estimate of mean surrounding bed elevation vary between studies and have included the following: a 1D transect upstream and downstream of the particle (Buffington et al., 1992; Kirchner et al., 1990), only elevations immediately downstream (Yager, Schmeeckle, & Badoux, 2018), only elevations in a 1D transect upstream (Smith et al., 2023), 2D areas upstream and downstream (Hodge et al., 2013), and 2D areas from different potential flow angles of attack (Hodge et al., 2020; Voepel et al., 2019). For the locally high bed elevation, the maximum upstream elevation in a 1D transect (Buffington et al., 1992; Kirchner et al., 1990), the 95th percentile of upstream elevations in a 1D transect (Hodge & Buechel, 2022) and the exposed area from complex 3D topography at various angles of attack have all been employed (Hodge et al., 2020; Voepel et al., 2019). Almost all surrounding bed elevations for protrusion estimates are within a distance equivalent to D_{84} (84th percentile of bed GSD) from the particle. This assumes that the downstream sheltering distance of an obstruction is similar to the bed roughness length, which is often represented by the D_{84} . However, a distance of 8–10 obstacle heights downstream of an obstruction may be needed for the flow to return to unobstructed values rather than just over one D_{84} (Heald et al., 2004; Schmeeckle & Nelson, 2003). In addition, for grains smaller than the D_{50} , protrusion may differ if calculated using immediately upstream elevations versus elevations averaged as far as 10 D_{50} upstream (Smith et al., 2023).

To address these limitations in measuring protrusion and subsequent uncertainties in calculated τ^*_c , we propose a new objective, fast, and automated method (Pro+) of obtaining protrusion and τ^*_c from point clouds or DEMs. Pro+ requires the bed topography in the format of a detrended (local streamwise bed slope removed) bed point cloud, the diameter of each grain, and either the perimeter of each grain or the portion of the point cloud corresponding to each grain (hereinafter called grain point cloud). The grain diameters and grain perimeters/point clouds can be obtained from a range of techniques such as deep learning or grain detection in point clouds (Butler et al., 2001; Chen et al., 2020; Steer et al., 2022; Walicka et al., 2021; Wu et al., 2021). For example, the software G3Point automates grain size measurements from 3D point clouds using flow routing algorithms and ellipsoidal fits to grains (Steer et al., 2022). We develop Pro+ using inputs from either G3Point or algorithms that output grain perimeters and grain sizes. Pro+ uses particle perimeters to determine the protrusion for each grain and calculates τ^*_c distributions for each grain size bin and the entire bed using a previously published force balance model (Yager, Schmeeckle, & Badoux, 2018).

We validate G3Point and Pro+ using manually estimated grain sizes and grain perimeters from orthomosaics of two laboratory experiments with different grain size distributions and bed topographies. We substitute the manually measured grain perimeters and sizes into the Pro+ code to calculate protrusion and τ_c^* distributions. We compare these grain size, protrusion and τ_c^* values to the fully automated values produced by the combination of G3Point/Pro+. Using Pro+, we also explore how protrusion distributions are influenced by the (1) distance over which surrounding bed elevations are measured, (2) representative surrounding bed elevation (e.g. median and maximum) used to define protrusion and (3) direction (upstream or downstream of particle) of surrounding elevations. We use this information to refine protrusion calculations and the force balance model in Pro+.

2 | METHODS

Our method section outlines (1) τ_c^* calculations and inputs as well as the associated protrusion definitions used in Pro+, (2) details of the automated protrusion measurements in Pro+, (3) two laboratory experiments, (4) manual measurements from the experiments, (5) testing Pro+ assumptions using manual measurements and (6) validating Pro+/G3Point using manual measurements. Steer et al. (2022) provide details on G3Point calculations including point cloud detrending (details provided in G3Point code), flow routing to initially define possible grain locations, algorithms to merge grains, and ellipsoidal fits to obtain grain sizes and grain point clouds.

2.1 | Pro+ automated τ_c^* estimates

In Pro+, we employ the force balance equations of Yager, Schmeeckle and Badoux (2018) because they represent the influence of bed structure on both applied fluid forces and resisting bed forces (see supporting information for full equations and Table S1 for inputs). The force balance requires grain size and protrusion. To measure protrusion, Pro+ needs inputs from either (1) G3Point, which provides the point cloud associated with each grain (grain point cloud) and grain size (see Table S2 for requirements), or (2) other software (see Section 1) that provides grain perimeter coordinates and grain sizes (see Table S3 for requirements). If using G3Point, Pro+ only employs grains that are well fit by ellipsoids according to G3Point standards (Steer et al., 2022). The intermediate grain axis (b) represents grain size in Pro+ because the force balance equations were derived assuming spherical grains. These equations calculate grain areas exposed to the flow and buried grain volumes that are not easily determined for ellipsoidal shapes. Almost all force balance equations for the onset of sediment motion make similar assumptions of spherical particle shapes (Buffington et al., 1992; Hodge et al., 2013; Hodge & Buechel, 2022; Kirchner et al., 1990; Lamb et al., 2008; Wiberg & Smith, 1987).

We alter the equations of Yager, Schmeeckle and Badoux (2018) to use two different protrusion definitions, one protrusion (p_D) that affects driving fluid forces and one (p_R) that affects forces resisting particle motion. Both p_D and p_R are the difference between the highest elevation on a particle and a representative surrounding bed

elevation, which differs between p_R and p_D . Pro+ determines p_R using the median surrounding bed elevation. Calculated resisting forces depend on p_R because of the (1) overburden weight caused by partial or full particle burial (i.e. burial = $b - p_R$) and (2) associated intergranular friction of the particle sliding past any burying grains. We assume that burial effects are likely caused by grains that occur at relatively high (average or greater) elevations surrounding the particle of interest to define p_R .

In contrast, we calculate p_D based on a low (10th) percentile of the surrounding bed elevations because of how flow velocities are calculated in Pro+. Instead of assuming a logarithmic velocity profile as in Yager, Schmeeckle and Badoux (2018), we use a hybrid mixing-length velocity profile equation that was specifically developed for the near-bed roughness layer (Lamb et al., 2017b). This equation provides a better estimate of the flow velocity (u) within the roughness layer and calculates the same u as that estimated by the logarithmic profile for vertical distances from the bed (z) that are much greater than the roughness length (k_s). We use the simplified version of the velocity profile equation for an impermeable bed (Equation 11 in Lamb et al., 2017b) in which $u = 0$ when $z = 0$. For p_D estimates, $z = 0$ should correspond to a low percentile of the surrounding bed elevation to allow the calculated u to be nonzero through most of the roughness layer. Details on Pro+ extraction of surrounding bed elevations are provided in the next section.

In the velocity profile equation, k_s is often assumed to be a function of D_{84} but the standard deviation of bed elevations (σ_z) could be more representative because it allows for the influence of other roughness sources beyond grains (Aberle & Smart, 2003; Bertin et al., 2017; Ferguson et al., 2019; Johnson, 2014, 2017; Powell et al., 2016; Schneider et al., 2015; Smart et al., 2002; Yochum et al., 2012). Given the uncertainties in k_s definition, Pro+ has three choices available for k_s : (1) a user specified value, (2) Pro+ calculated D_{84} from the input GSD, or (3) Pro+ calculated σ_z from the input detrended bed point cloud.

Finally, pivot (ϕ_p) and intergranular friction angles (ϕ_f) are used in the force balance equations but are difficult to directly measure and are therefore assumed in Pro+. Either a single value or a normal distribution of ϕ_f can be used; the mean, standard deviation and number of random samples of the distribution are required inputs. Pro+ can either effectively neglect pivot angle effects (see supporting information for details) or can use a ϕ_p distribution, which is obtained from Equation (4) in Kirchner et al. (1990). This equation has considerable uncertainties and may only be valid for certain percentiles of the distribution (see Kirchner et al. [1990] for details). In addition, one study found that ϕ_p may not exert a strong mechanistic control on τ_c^* (Hodge et al., 2020).

In summary, Pro+ calculations of τ_c^* employ assumed constants (e.g. drag coefficients), ϕ_p , ϕ_f and k_s values as well as measurements of b , p_D and p_R for each grain on the bed. A complete list of input requirements for Pro+ is provided in the supporting information (Table S1). If a single value of ϕ_f and no ϕ_p is used, then Pro+ will obtain a single value of τ_c^* for each particle. If distributions of ϕ_f and ϕ_p are used, then each individual grain will have a distribution of potential τ_c^* values because of these assumed angle distributions (see Yager, Schmeeckle, & Badoux, 2018 for details). Pro+ combines all p_D , p_R and τ_c^* values for particles within each grain size bin to determine the distribution of p_D , p_R and τ_c^* for each representative grain size.

Such τ^*_{ci} values for each grain size could be used to create hiding functions. All available p_D , p_R and τ^*_c are also combined to obtain these distributions for the entire bed (see Table S4 for a full list of Pro+ outputs). Application of these full τ^*_{ci} distributions, or single representative values of each τ^*_{ci} distribution, in bedload transport predictions is examined in the discussion section.

2.2 | Pro+ automated protrusion estimates

We now outline the details of Pro+ calculations of protrusion (p_D and p_R), which require the point cloud associated with each grain (grain point cloud) and the grain perimeters in x and y coordinates (streamwise and cross-stream). A high-resolution DEM could also be employed for this analysis if the DEM is converted to a point cloud format, which is required in both the G3Point and Pro+ codes. The two potential software inputs (G3Point or other software) to Pro+ either provide the grain point cloud or the grain perimeter and therefore Pro+ calculations differ slightly depending on the pre-run software (Figure 1). If using G3Point to input individual grain point clouds, Pro+ calculates the perimeter of each particle as the outer planform boundary of the provided particle point cloud. This allows for irregular grain perimeters that closely track the actual grain shape (Figure 2). If grain perimeters are instead input from other software, Pro+ determines the point cloud of each grain using these perimeters and the provided detrended bed point cloud.

The remaining calculations are the same regardless of the pre-run software inputs to Pro+ (Figure 1). Pro+ determines the maximum elevation of every particle from each particle point cloud. A horizontal search distance must be input for Pro+ to identify the surrounding bed elevations around each particle. Similar to k_s , the search distance should be partly informed by the expected sheltering distance from surrounding obstacles. Force chains, which mechanistically influence resisting forces and are composed of structures of grains that are held together by large forces, can also extend considerable distances from particles (Bi et al., 2011; Daniels et al., 2017). The Pro+ options for defining the search distance are therefore the same as those for k_s : a user specified value, D_{84} or σ_z . The surrounding bed elevations include all points within the bed point cloud that are within the search distance, which starts at the grain perimeter. The irregularly shaped surrounding bed area closely mimics the grain shape (Figure 2). We included all elevations within this bed area rather than just those only upstream or downstream of the grain because of the potential importance of (1) different flow directions on driving forces and (2) all locations around the particle in controlling resisting forces (Hodge et al., 2020; Voepel et al., 2019; Yager, Schmeeckle, & Badoux, 2018). The 10th and 50th percentiles of the surrounding bed elevations are subtracted from the maximum grain elevation to determine p_D and p_R , respectively. We evaluate various assumptions in the protrusion calculations using data collected in laboratory experiments (see next three sections).

2.3 | Laboratory experiments

To test assumptions in Pro+ and to validate Pro+ and G3Point outputs, we conducted two experiments in the Center for Ecohydraulics

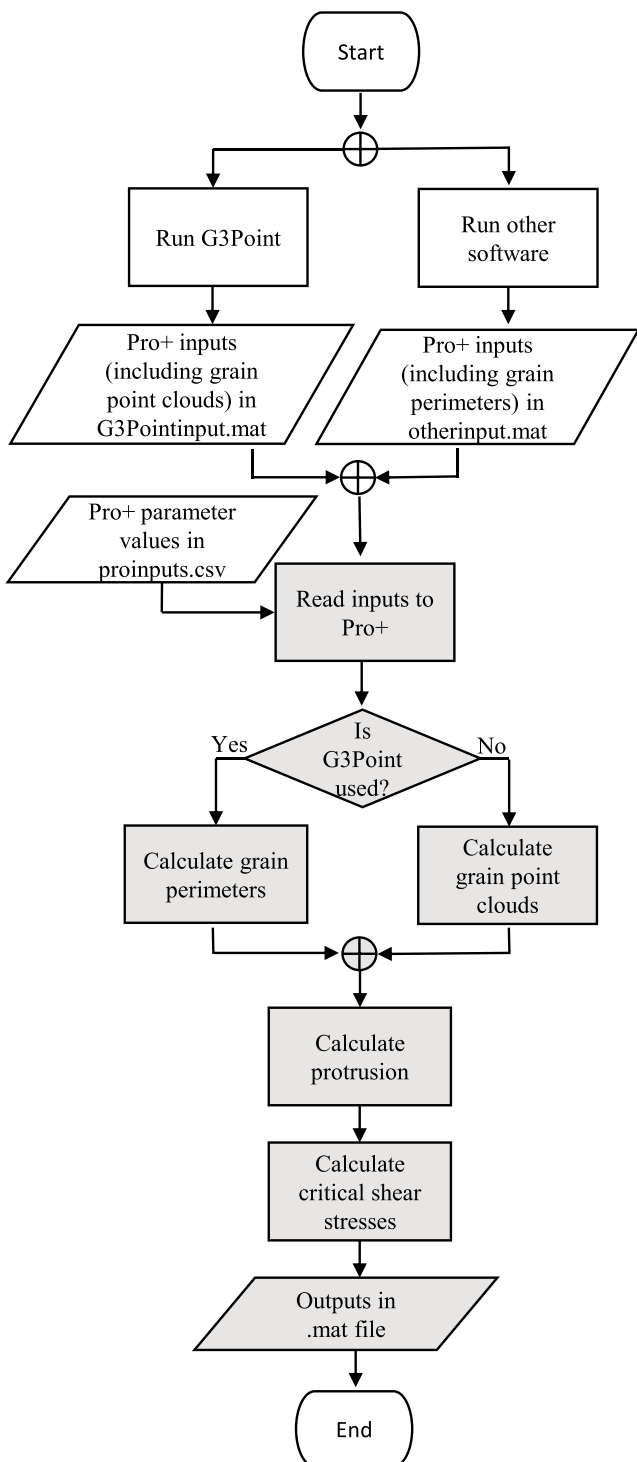


FIGURE 1 Flow chart of the necessary calculations and inputs before (white) running Pro+ and a broad overview of calculations within Pro+ (grey).

Research (CER) Mountain Streamlab, which is a 20-m long and 2-m wide flume with an adjustable slope that was set to 1.15% (Budwig & Goodwin, 2012). In both experiments, a bulk sediment mixture consisted of 10% 0.5 mm sand and 90% gravel with a D_{50} of 11 mm. Further details on the sand and gravel particle shapes are provided in Yager, Venditti, et al. (2018). We varied the gravel sorting parameter ($\sigma_g = [D_{84}/D_{16}]^{0.5}$ where D_{16} is the 16th percentile of the gravel distribution) of the bulk gravel mixture between experiments to create a narrow ($\sigma_g = 1.23$) or wide ($\sigma_g = 2.71$) bulk gravel size distribution

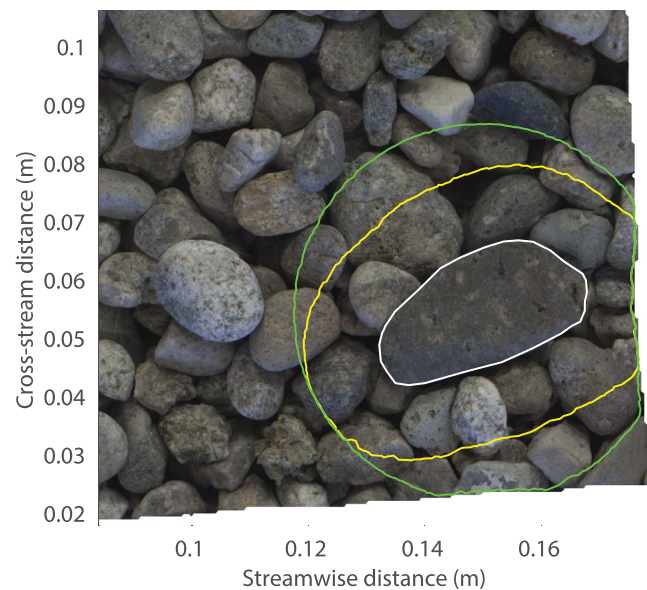


FIGURE 2 Example surrounding bed area used to calculate protrusion for one grain. The grain perimeter shape is shown in white, and the farthest extent of the irregular and circular shaped searches are shown in yellow and green, respectively, for an example search distance of 0.013 m. Points are included in the surrounding bed area if they are between the white grain perimeter and the respective coloured line.

that can influence particle protrusion (Kirchner et al., 1990; Smith et al., 2023). The narrow GSD experiment had a bulk mixture D_{16} , D_{84} and D_{\max} (maximum size) of 9, 14 and 31 mm, respectively, whereas the wide GSD bulk mixture had values of 4, 30 and 63 mm, respectively.

The narrow GSD experiment was not water worked, whereas the wide GSD experiment was water worked without any upstream sediment supply to create a well-developed armour layer. The experiments were not scaled to a specific prototype, and we used different GSD and bed preparation techniques (screeded vs. water working) to vary potential particle arrangements and bed topographies (Masteller & Finnegan, 2017; Ockelford & Haynes, 2013), which could affect GSD accuracy from G3Point and protrusion accuracy from Pro+. An adjustable tailgate at the end of the flume ensured uniform flow during water working, which was validated with flow-depth measurements throughout the flume length. Water working consisted of a 12-h long flow at a constant discharge of 0.7 m³/s that visibly moved the bulk mixture D_{84} in preliminary experiments. This was followed by a 4-h long flow (0.5 m³/s) that visibly moved the bulk mixture D_{50} in preliminary experiments and preferentially transported fine sediment into the bed or out of the flume. Similar sequences of flows have armoured beds in previous laboratory experiments (Curran & Waters, 2014). We spray painted the armour layer in a 1-m long by 1.5-m wide area, removed all spray-painted grains, and sieved these grains at half-phi intervals. The armour layer D_{16} , D_{50} and D_{84} for the wide GSD experiment were 8, 18 and 32 mm (resulting in $\sigma_g = 1.95$) with less than 1% sand. We only focus on gravel sized particles because G3Point cannot accurately quantify sand (see Steer et al., 2022).

In the narrow and wide GSD experiments, we photographed the bed surface after placing the bulk sediment mixture in the flume

or after water working, respectively. A high-resolution camera (Blackfly 5Mpix; focal length of 12.5 mm; ~20 cm from bed; ~0.05 mm/pix) photographed many (156 in wide GSD or 195 in narrow GSD) images with at least 60% overlap from various angles relative to the bed and around the area of interest (15 m downstream of flume entrance). Each set of photographs contained a carpenter's square that provided scale bars in multiple directions needed for scaling the topography. The photos were used in Structure from Motion (SfM) photogrammetry analyses (Agisoft Metashape professional version 1.5.1) to create scaled point clouds for G3Point/Pro+ measurements and scaled orthomosaics for manual measurements. The original point clouds had an average resolution finer than 0.2 mm (Figure 3) that was decimated to a resolution of 0.4 mm, which enabled use in G3Point (see Steer et al., [2022] for limitations on point cloud size) and facilitated faster calculations in Pro+.

2.4 | Grain measurements

We needed independent estimates of grain size, protrusion, and τ^*_{c} to validate G3Point/Pro+, but different measurement techniques can produce values that are not always directly comparable (Hodge et al., in review). For example, sieved bulk bed samples, pebble counts and photogrammetry can provide differing GSD because of spatial variability in sample locations and methodological differences/errors. Protrusion from rulers or point gages, computerised tomography (CT) scans and Pro+ could also differ because of inconsistent sampling of surrounding bed elevations (Hodge et al., in review). Finally, estimated τ^*_{c} are known to vary with measurement method (e.g. bedload samples and tracers) and onset of motion definition (Buffington & Montgomery, 1997). To use the same (or similar) techniques/definitions between our validation measurements and G3Point/Pro+, we manually identified and measured grains in the orthomosaic images.

To keep the number of manually digitised grains manageable, we subsampled the point clouds and corresponding orthomosaics to smaller representative areas (0.12 × 0.14 m vs. 0.15 × 0.35 m for narrow vs. wide GSD experiments) (Figure 3). Different shaped areas were used because of the different grain sizes and orientations between the two experiments; capturing the largest grains in the wide GSD experiment required using a more rectangular area that mimicked the orientation of these particles. For a given experiment, these smaller areas had the same σ_z as the entire bed shown in Figure 3 and were therefore topographically representative. We manually measured the visible b axis and digitised the perimeter of every grain visible in the orthomosaic images, which resulted in 181 and 302 measured grains for the narrow and wide GSD experiments, respectively. Therefore, the chosen areas also provided a sample size large enough to determine the GSD. We substituted the manually measured perimeters in the Pro+ code in place of the G3Point/Pro+ perimeters to calculate 'manual-based' p_D and p_R values and evaluate Pro+ assumptions (Section 2.5). We also used these manual perimeters and grain sizes in the Pro+ code to determine how grain identification errors in G3Point propagated to errors in G3Point/Pro+ estimated grain size, protrusion, and τ^*_{c} values (Section 2.6).

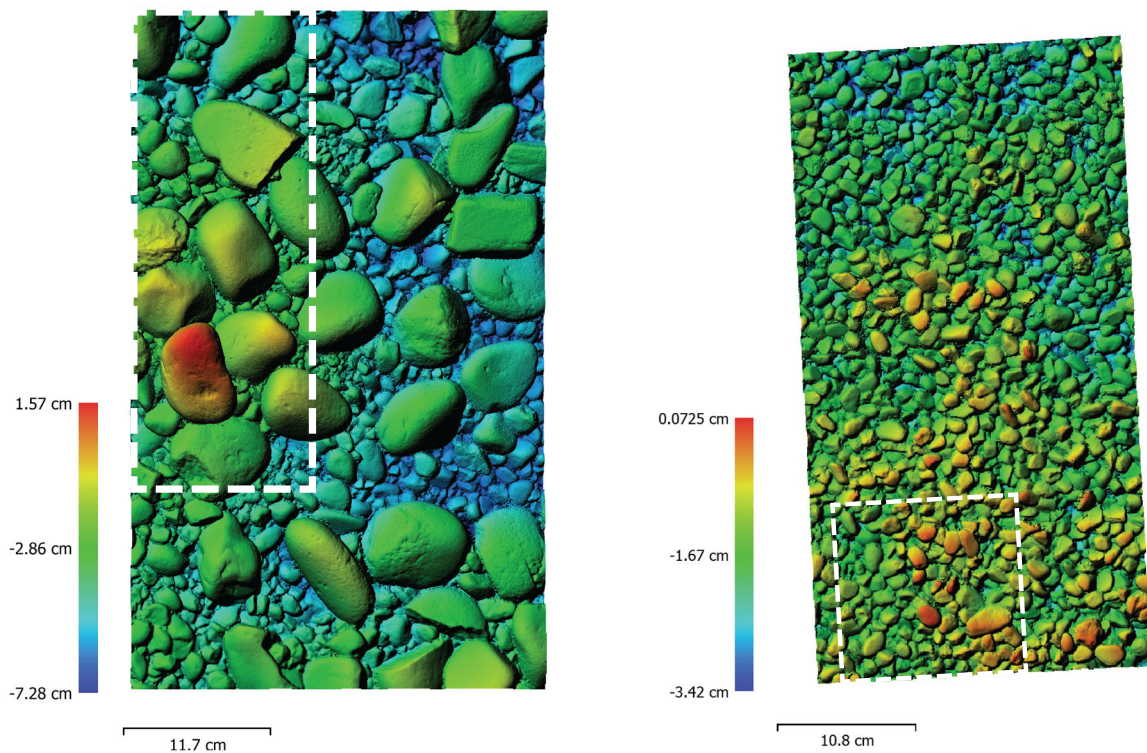


FIGURE 3 DEMs of the (left) wide GSD experiment after water working and (right) narrow GSD experiment without water working. White dashed boxes outline the areas in each experiment used in the G3Point/Pro+ validation and contained (right) 181 and (left) 302 manually measured grains.

2.5 | Testing Pro+ assumptions

Before validating Pro+, we needed to test several assumptions and calculation methods. For all calculations in this section, we used the manual measurements in the wide GSD experiment as an example. Pro+ uses two different representative surrounding bed elevations (10th and 50th percentiles, p_D and p_R) to define protrusion. But in previous studies (see Section 1), the representative bed elevation(s) is usually (1) only the median or average, (2) only a high percentile (e.g. 84th or 90th), or (3) a combination of the median or mean (projection) and a high percentile (exposure). We therefore calculated protrusion using the 10th (p_D), 50th (p_R) and 84th (no associated Pro+ protrusion variable) percentiles of the surrounding bed elevations to determine how they affect protrusion distributions.

We also investigated the influence of the surrounding bed search area shape, search distance and search location. Our irregularly shaped search area can be computationally expensive, and we therefore tested a more efficient simple circular search distance that starts at the grain centroid (Figure 2). To enable comparison with the irregularly shaped search that starts at the grain perimeter, the actual search distance for the circular shape was the grain b axis plus the specified search distance magnitude. Similar to the irregularly shaped search, the circular search also excludes any points occupied by the grain of interest. We investigated the influence of these two different search shapes (irregular vs. circular) on p_D and p_R distributions for a range of specified search distances. Finally, previous protrusion estimates (see Section 1) use different surrounding bed locations (upstream, downstream, all) relative to the grain of interest. We therefore evaluated using only points in the surrounding bed search that were upstream or downstream of a flow perpendicular line through the grain centroid

to calculate p_D and p_R distributions. Both upstream and downstream areas are extended along the grain sides to the grain centroid.

2.6 | Validating G3Point and Pro+

After testing assumptions in Pro+, we then used the manual-based b , p_D and p_R distributions from both experiments to validate G3Point/Pro+. We substituted these manual-based b , p_D and p_R distributions into the τ_c^* calculations in Pro+ to obtain τ_c^* distributions, which are hereinafter also called ‘manual-based’ τ_c^* values for simplicity. Given that differences in dimensional critical shear stresses (τ_c) are intuitively easier to compare than dimensionless values, we convert all τ_c^* values to τ_c using Shields equation.

To compare G3Point/Pro+ outputs with these manual-based b , p_D , p_R and τ_c distributions, we first ‘calibrated’ tunable G3Point input variables using the trial-and-error approach of Steer et al. (2022) on the subsampled point clouds (Figure 3). Most researchers lack manually estimated grain perimeters and therefore manual-based protrusion and τ_c estimates for explicit Pro+ testing/calibration. We therefore focussed only on G3Point calibration using measured GSD and grains visible in orthomosaics. We adjusted several G3Point inputs to provide (1) reasonably accurate fits to manual GSDs (Steer et al., 2022) and (2) the most visually comparable grain perimeters to those on the orthomosaics. These adjustable input variables were the minimum number of points that should contain a grain (n_{min}), scaling factor to determine grain merging (C_F), two different angles (between the normals of grain crest points) below which two grains are merged (α, β), and threshold flatness below which to remove a grain (ϕ_{flat}). We then fixed these input variables for a given experiment and explored a

range of G3Point k values, which is the number of nearest neighbours for the flow routing algorithm and strongly controls G3Point accuracy (Steer et al., 2022).

Goodness of fit between the G3Point and manual GSD was determined using p -values from a two-sample Kolmogorov–Smirnov test ($\alpha = 0.05$) and percent errors in certain GSD percentiles. For a range of k values, we highlight the results from the G3Point input variable combination that produced high p values and low percent errors for GSD in each experiment. Percent errors in the 10th, 50th, and 90th GSD percentiles were the absolute value of the difference between the manual and G3Point estimate divided by the manual estimate. We also calculated the p -values and percent errors for protrusion and τ_c distributions using a range of k values and the optimal G3Point input variable combination in each experiment.

The direct ellipsoid fitting method in G3Point did not perform well in our experiments, and we only discuss the inertial fitting method. The default G3Point methodology of removing minima from the point cloud caused many grains in locally flat areas to be mis-identified, and we did not remove minima in our calculations. Further details on ellipsoid fitting methods and G3Point input variables are provided in Steer et al. (2022).

To calculate protrusion, we used the irregular search shape (Figure 2) with an example search distance of 0.014 m in both our manual-based and G3Point/Pro+ validation calculations. The search distance needed to accurately define protrusion is still an open question in the literature (Smith et al., 2023) and, as discussed above, is likely related to the D_{84} or σ_z . For the narrow GSD experiment, the search distance of 0.014 m equaled the bulk mixture D_{84} and was far greater than the σ_z of 0.004 m. In the wide GSD experiment, our search distance equaled σ_z . We could not use a search distance that equaled the D_{84} (0.032 m) of the wide GSD experiment because 0.032 m was larger than the x dimension of our test area (Figure 3). In both the G3Point/Pro+ and manual-based τ_c validation estimates, we used $k_s = \sigma_z$ of the detrended point cloud in each experiment, ϕ_f set to 60°, and no ϕ_p . Preliminary tests showed that using distributions of ϕ_f and ϕ_p artificially inflated the τ_c sample size in statistical comparisons compared to using single values of these angles.

3 | RESULTS

We first use the manual-based protrusion estimates to investigate protrusion sensitivity to the representative surrounding bed elevation, search shape, search distance and search location (Section 3.1). We then test G3Point/Pro+ b , p_R , p_D and τ_c distributions against the manual-based distributions in both experiments (Sections 3.2 and 3.3).

3.1 | Protrusion sensitivity

We use the manual-based protrusion distributions for the wide GSD experiment as representative examples to test protrusion sensitivity. We first examine sensitivity of the p_R and p_D distributions in each grain size bin to the search shape and search distance (varied between 2 and 16 mm). For simplicity, we report medians of the p_R and p_D distributions in example end-member (2 and 55 mm) and intermediate

(7 and 19 mm) grain size bins. For a given search distance and grain size, the circular search shape systematically under-estimated median p_R and often over-estimated median p_D compared to the irregular search shape (Figure 4c and d) that mimicked the shape of the grain. The underestimation of median p_R by the circular search shape also increased with greater particle size (Figure 4e). The circular search shape could therefore cause systematic biases in calculated τ_c changes with grain size. We concluded that such biases outweighed potential efficiency benefits, and this shape is not included in Pro+ or in our remaining analyses.

For the irregular search shape, median p_R and p_D for most grain sizes were relatively constant with search distance (Figure 4c and d). Two exceptions were that a greater search distance caused median p_R to decrease for smaller grains (e.g. 2 and 7 mm in Figure 4d) and median p_D to slightly increase for larger grains (e.g. 19 and 55 mm in Figure 4c). Given the relative insensitivity of protrusion to search distance, we used a search distance of 0.014 m (see Methods) in all subsequent calculations. We also investigated the role of search location because many studies use different locations (e.g. upstream, downstream, all) of surrounding bed elevations to calculate protrusion. As an example, we show the median p_D for each grain size bin calculated using only upstream or downstream locations. Median p_D was not systematically greater when using either the upstream or downstream locations (Figure 4f). Differences in median p_D between upstream and downstream locations also did not systematically change with grain size. Regardless of employed location, the median p_D increased with coarser grain sizes as expected (Kirchner et al., 1990; Smith et al., 2023). We conclude that using the entire search area is appropriate given that upstream and downstream protrusion values did not display any systematic differences in our analyses.

We finally assessed the impact of the representative surrounding bed elevation on protrusion. The 50th percentile of the surrounding bed elevation is commonly used (see Section 1) but produced a protrusion distribution (p_R) in which nearly half of the values were negative (Figure 4a). A higher representative surrounding bed elevation (e.g. 84th percentile) caused even more negative protrusion values (not shown). Negative values of p_R still have calculated resisting forces because they result in a fully buried grain ($p_R < 0$ reverts to $p_R = 0$ in Pro+ calculations). However, grains with negative protrusions do not have calculated exposed areas to flow, experience zero calculated flow velocities when using velocity profile equations, and have zero calculated lift and drag forces. Therefore, the common methodology of using the 50th percentile (or higher) of the surrounding bed elevation in driving force calculations would result in a large proportion of grains (see cartoon in Figure 4a) without a calculated τ_c value. The reference bed elevation where $u(z) = 0$ for p_D should instead be a low percentile of the distribution that allows for most grains to have calculated velocities, exposed areas, driving forces and τ_c values. The 10th percentile of the surrounding bed elevation produced a low percentage of negative protrusions (p_D) (Figure 4a), which allowed us to calculate driving forces and τ_c for most grains. For example, replacing p_D with p_R in calculations of τ_c for the wide GSD experiment resulted in only 133 grains having an estimated τ_c instead of 253 grains when using both p_D and p_R . Only using p_R also caused systematically larger τ_c values than if both p_D and p_R were used (Figure 4b).

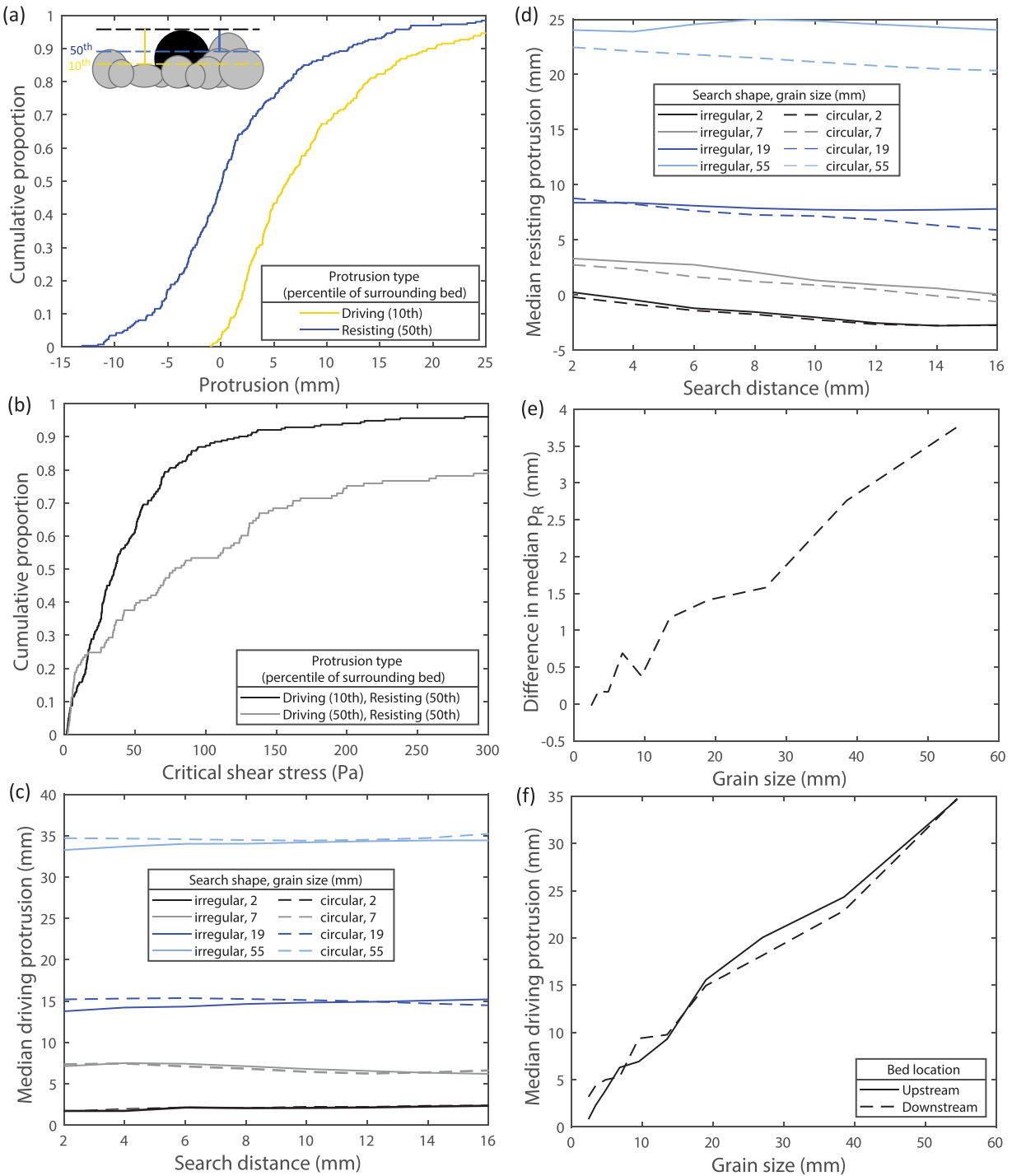


FIGURE 4 Sensitivity of manually measured protrusion values for the wide GSD (grain size distribution) experiment. (a) Protrusion distributions for all grains using an irregular search shape and the 10th (driving protrusion, p_D) and 50th (resisting protrusion, p_R) percentiles of the surrounding bed elevation. Inset cartoon shows example p_R (blue line) and p_D (yellow line) for the black grain. All grains below the local (grain and search radius dependent) 50th percentile bed elevation would have negative p_R and are shown in light grey. (b) Calculated critical shear stresses for all grains using p_R and p_D from (a) or by replacing p_D with p_R in all calculations. (c) Median p_D and (d) median p_R as functions of search distance and search shape (different line types) for example grain sizes (line colours, labelled with average grain size in bin). (e) The difference between the median p_R calculated using an irregular search shape and the median p_R calculated using a circular search shape for each grain size bin. (f) Influence of upstream and downstream search location on median p_D for each grain size bin using an irregular search shape. Figure 4a and b and Figure 4e and f use a search distance of 0.014 m.

3.2 | G3Point validation

To assess G3Point accuracy, we now compare the G3Point and manual GSD in each experiment and compare G3Point grain perimeters to grains visible in the orthomosaics. We discuss the optimal G3Point

input variable combination in each experiment (see Table 1) for a range of possible input G3Point k values (see Section 2). In each experiment, G3Point produced a GSD (Figure 5a and d) that closely resembled the shape of the manually estimated distribution for most tested k values. Certain k values also produced generally low GSD

TABLE 1 Accuracy of G3Point/Pro+ grain size (b), driving protrusion (p_D), resisting protrusion (p_R), and τ_c distributions in each experiment (narrow vs. wide grain size distributions (GSD)).

Experiment (example k value)	p-value				Percent error in 10th, 50th, 90th percentiles			
	b	p_D	p_R	τ_c	b	p_D	p_R	τ_c
Narrow GSD ($k = 30$)	0.51	0.82	0.95	0.04	11, 4, 14	13, 5, <1	367 ^a , 5, <1	49, 20, 8
Narrow GSD ($k = 40$)	0.20	0.97	0.91	0.002	17, 9, 8	11, 4, 3	354 ^a , <1, <1	61, 28, 19
Wide GSD ($k = 10$)	0.03	0.89	0.48	0.66	3, 13, 18	2, 4, 11	7 ^a , 322 ^a , 23	48, 8, <1
Wide GSD ($k = 15$)	0.15	0.82	0.69	0.002	20, 14, 9	4, 5, 5	7 ^a , 193 ^a , 13	115, 39, 51

Note: Two example G3Point k values are shown for each experiment using the optimal G3Point input variable combination, which was assessed using p -values and percent errors for each output variable (b , p_D , p_R and τ_c).

^aDenotes that manual-based and/or G3Point/Pro+ p_R estimates were negative and were converted to zero values in τ_c calculations. Optimised G3Point input variables for the narrow GSD ($n_{\min} = 50$, $C_F = 0.1$, $\alpha = 10^\circ$, $\beta = 10^\circ$, $\phi_{\text{flat}} = 0.1$) and wide GSD ($n_{\min} = 10$, $C_F = 0.1$, $\alpha = 60^\circ$, $\beta = 20^\circ$, $\phi_{\text{flat}} = 0.1$) experiments were used in Table 1 and Figures 4–6, 7a–c, and 8.

percent errors (Table 1; less than ~15%) in each experiment. These k values mostly produced relatively high GSD p -values (e.g. $p > 0.05$), which implies that G3Point GSD and manual GSD may not be statistically different within the uncertainties of the distributions. Some optimal G3Point input variables were the same between experiments (C_F , ϕ_{flat}), whereas others differed (n_{\min} , k , α , β) (see Table 1), which suggests that G3Point GSD calibration may be needed in individual rivers with distinct grain sizes, grain shapes or topographies.

G3Point accurately identified the locations and approximate perimeters of many grains but sometimes lumped grains together or split grains into multiple particles, even using the optimal G3Point input variables (Figures 6 and 7). For the optimal G3Point input variables, k altered the relative number of lumped or split grains but could not eliminate either problem (Figure 6b vs. 6c; Figure 7b vs. 7c). In the wide GSD experiment, G3Point also misidentified small particles sitting on top of large relatively flat grains (Figure 7). Other G3Point input variable combinations also produced reasonable GSD with low percent errors and high p -values but had greater grain identification/perimeter errors than our optimal input variable values (Figure 7d).

3.3 | Pro+ validation

We now use the range of G3Point k values and the optimal G3Point input variable combination from the last section in Pro+ to calculate p_D , p_R and τ_c distributions. For all tested k values, G3Point/Pro+ p_D and p_R distributions closely mimicked the shape of the manual-based protrusion distributions in each experiment (Figure 5b and e). This is further supported by relatively high p -values for p_D and p_R in both experiments (Table 1), implying G3Point/Pro+ and manual-based protrusion distributions may not be statistically different within the distribution uncertainties. Although all percent errors for the G3Point/Pro+ p_D distributions were low, percent errors for the 10th or 50th percentiles of the G3Point/Pro+ p_R distribution were often large (Table 1). These percentiles had negative G3Point/Pro+ and/or manual-based protrusion values (see Figure 4a for example), which are automatically set to zero in the τ_c calculations (see supporting information). Therefore, some of the G3Point/Pro+ p_R errors did not propagate to τ_c .

The G3Point/Pro+ and manual-based τ_c distributions had similar shapes in the wide GSD experiment (Figure 5f) and some small shape

discrepancies (e.g. use of a single k value cannot fully match the manual distribution) in the narrow GSD experiment (Figure 5c). In each experiment, these visually similar G3Point/Pro+ and manual-based τ_c distributions were only statistically similar within the distribution uncertainties (high p -values) for some of the tested k values (Table 1). This implies that obtaining similar manual-based and G3Point/Pro+ τ_c distributions may be more difficult than obtaining similar grain size and protrusion distributions. Indeed, the percent errors in the G3Point/Pro+ τ_c distributions also strongly depended on k and were relatively high compared to those for grain size and some protrusion percentiles (Table 1).

4 | DISCUSSION

4.1 | Future work to test and improve Pro+

We used two laboratory experiments with different GSD and bed topographies to validate Pro+ sensitivity to input G3Point grain sizes and grain locations. Our results demonstrate that generally reasonable G3Point/Pro+ protrusion and τ_c distributions can be obtained by optimising only the GSD in G3Point. G3Point/Pro+ τ_c generally had larger errors than G3Point/Pro+ protrusion or G3Point grain size because the τ_c equation nonlinearly combines b , p_D and p_R uncertainties. Some of the differences between G3Point and manual GSDs can be attributed to errors common to photogrammetry measurements (Buscombe et al., 2010; Buscombe & Masselink, 2009; Garefalakis et al., 2023; Graham, 2005) such as partly buried grains, difficulty in identifying the b axis in 2D images, and vertically angled b axes that cause over- or under- estimation of axis length. However, most errors were largely caused by G3Point misidentified grain boundaries and locations (Figures 6 and 7). In particular, reasonably accurate grain size and protrusion distributions could be obtained by G3Point input variable combinations that produced very inaccurate grain perimeters (Figure 7d). G3Point can obtain the correct GSD for the wrong reasons, and we recommend using a combination of quantitative GSD errors and qualitative visual grain perimeter assessment in validation and calibration of G3Point.

Instead of using G3Point, Pro+ also has the option of inputting a detrended point cloud (or DEM in the format of a detrended point

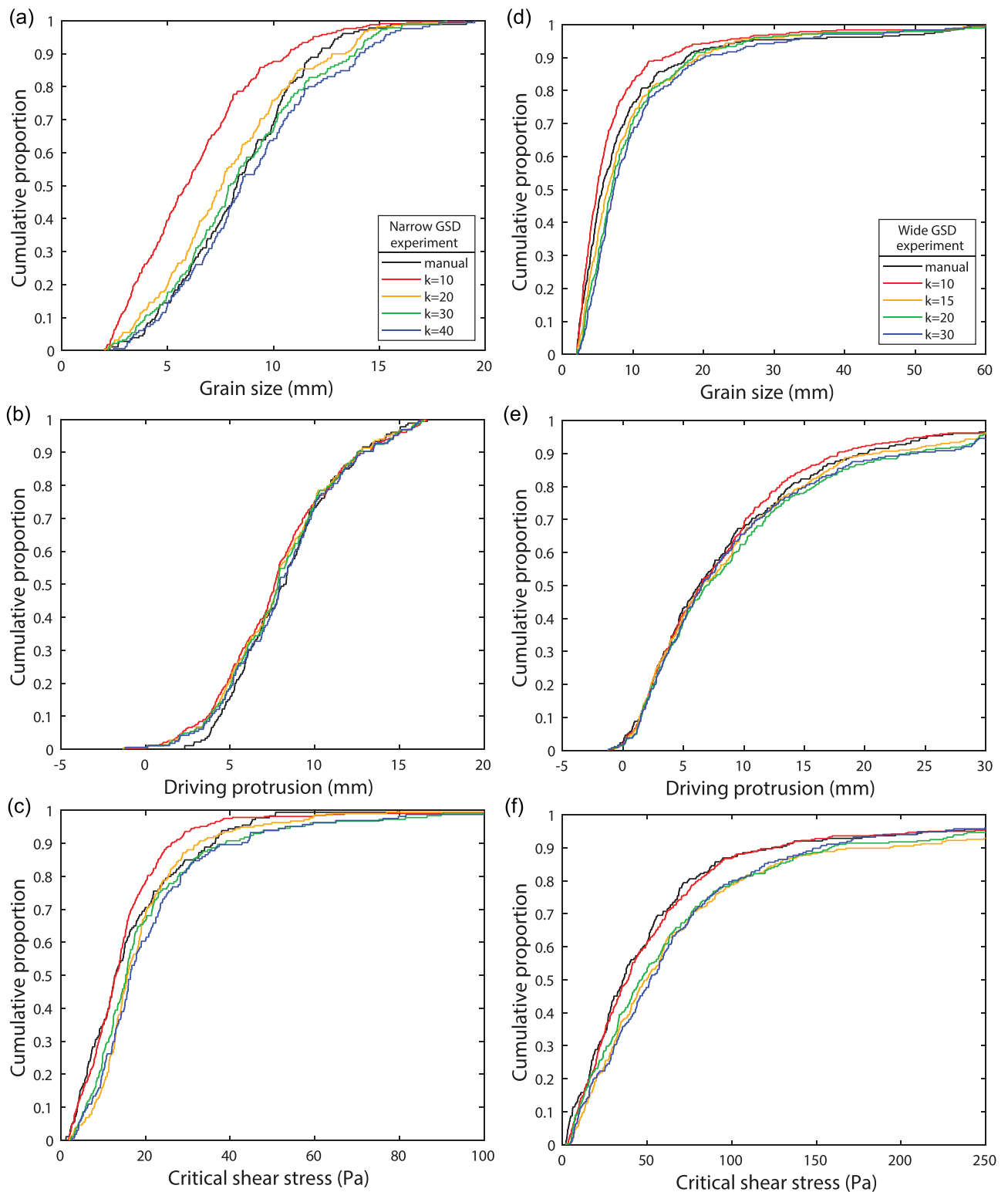


FIGURE 5 Comparison of manual-based (black lines) and G3Point/Pro+ (coloured lines labelled with G3Point k value) values for the (left column) narrow GSD (grain size distribution) experiment and (right column) wide GSD experiment. Each panel shows (a, d) grain size, (b, e) driving protrusion and (c, f) critical shear stress distributions. Legends in the top figure panels apply for the rest of each column. G3Point/Pro+ distributions are shown for the G3Point input variable combination (provided in Table 1) that optimised G3Point GSD and grain perimeter accuracy.

cloud), grain sizes and grain perimeter coordinates from other software. For example, deep learning can automatically identify grain perimeters and grain sizes in georeferenced orthomosaics from drone flights (Chen et al., 2020). Other methods based on point clouds or DEMs could also provide the necessary Pro+ inputs such as that of

Wu et al. (2021), which uses factorial kriging to identify grain edges in DEMs. Butler et al. (2001) also uses a variety of methods employing orthophotographs, DEMs, watershed segmentation, and ellipsoidal fits to detect grain perimeters and sizes. The Meta-developed Segment Anything Model (SAM) with specific application to grain detection

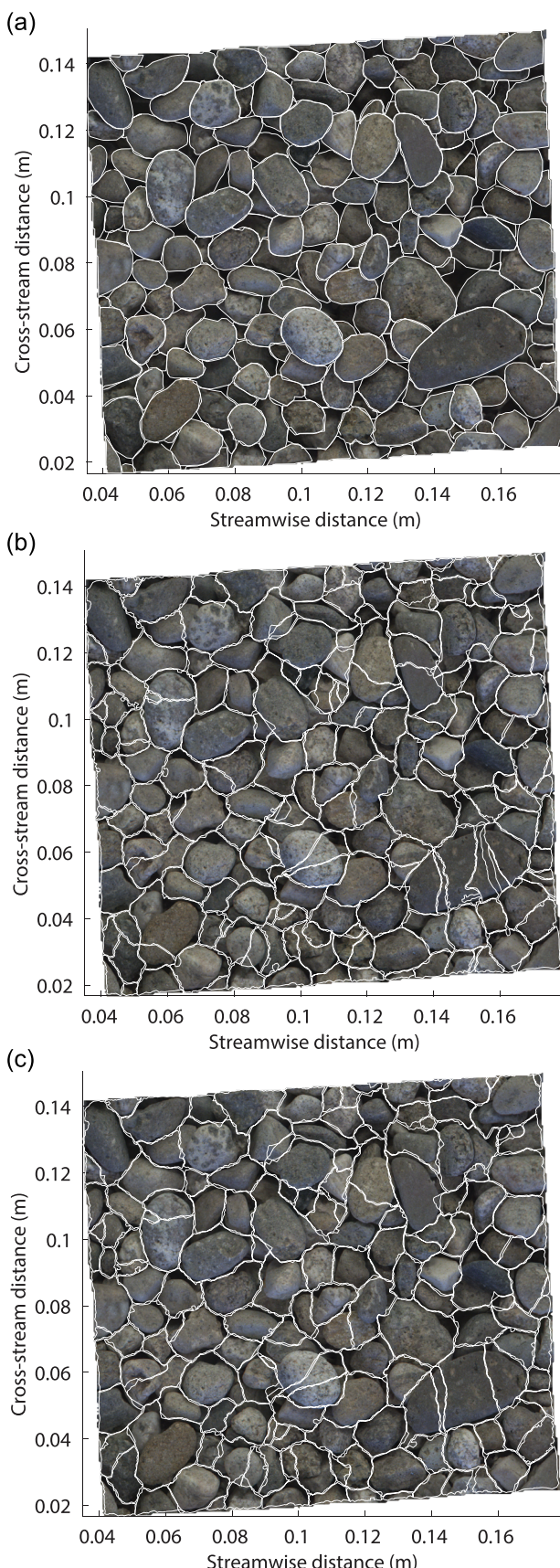


FIGURE 6 Orthomosaics of bed areas used in G3Point/Pro+ validation for the narrow GSD (grain size distribution) experiment. Bed areas are the same as those in the white boxes in Figure 1. White lines show (a) manual grain perimeters and (b, c) example grain perimeters from the optimal G3Point input variable combination (see Table 1) with a k value of (b) 30 and (c) 40.

through the ‘segmenteverygrain’ python package could be promising with modifications to export the grain perimeter coordinates needed by Pro+. Further Pro+ testing using various input software would be beneficial.

Beyond testing Pro+ sensitivity to input grain sizes and grain perimeters, comparisons are needed between Pro+ protrusion and τ_c distributions and those from direct measurements. For example, Hodge et al. (in review) compared Pro+ protrusion values to those measured using a ruler in the field and those measured using 3D CT scan data. All tested methods produced similar normalised protrusion (protrusion/grain size) values in each of the eight different sediment patches. However, the pattern of normalised protrusion between the patches was not consistent for the different methods, suggesting that different protrusion methods/definitions may complicate validation of Pro+.

For τ_c^* , such comparisons are further complicated because Pro+ provides a τ_c^* , τ_{ci}^* and/or τ_{c50}^* distribution, whereas most direct estimates only have one value. A low percentile (e.g. 1–10) of the calculated τ_{ci}^* or τ_{c50}^* distribution is often recommended because it corresponds to easily mobile grains that would be measured in bedload samplers or through particle motions (Buffington et al., 1992; Buxton et al., 2015; Kirchner et al., 1990). The exact percentile could be informed by future research comparing Pro+ τ_{ci}^* or τ_{c50}^* distributions to directly measured values. Encouragingly, force-balance equations can provide τ_c^* within the range of values determined using reference transport or flow competence approaches (Buffington et al., 1992; Hodge et al., 2013, 2020; Kirchner et al., 1990; Lamb et al., 2008; Wiberg & Smith, 1987). However, different τ_c^* values even occur between the direct reference transport rate and competence methods; each method involves a unique set of uncertainties and limitations that will also complicate Pro+ comparisons (Buffington & Montgomery, 1997; Smith et al., 2023; Wilcock, 1993).

In addition to further Pro+ validation, future research could focus on better characterising protrusion and the flow field needed for τ_c^* calculations. We used two representative surrounding bed elevation percentiles, 10th for p_D and 50th for p_R , to capture the different impacts of protrusion on driving and resisting forces, respectively. Previous studies often only use the median (or higher) surrounding bed elevation that may result in many negative protrusion values for which calculated flow velocities and driving forces are zero. Particles below the median bed elevation can actually experience positive time-averaged flow velocities because of the complex flow and pressure field driven by sheltering obstacles. Particles with zero protrusion also could have higher lift forces than those that protrude high into the flow column (Schmeeckle et al., 2007). Although spatially averaged sheltering effects are partly and indirectly included in the velocity profile for the roughness layer (Lamb et al., 2017b), the local flow fields that cause measurable drag and lift forces for very low or negative protrusion grains are not included in simple force balances. More studies are needed that measure/model the complex near-bed flow field over the rough topographies typical of gravel-bedded rivers (Curran & Tan, 2014; Lacey & Roy, 2007; Monsalve et al., 2017; Strom & Papanicolaou, 2007). Such information could be used to improve the flow equations employed in Pro+.

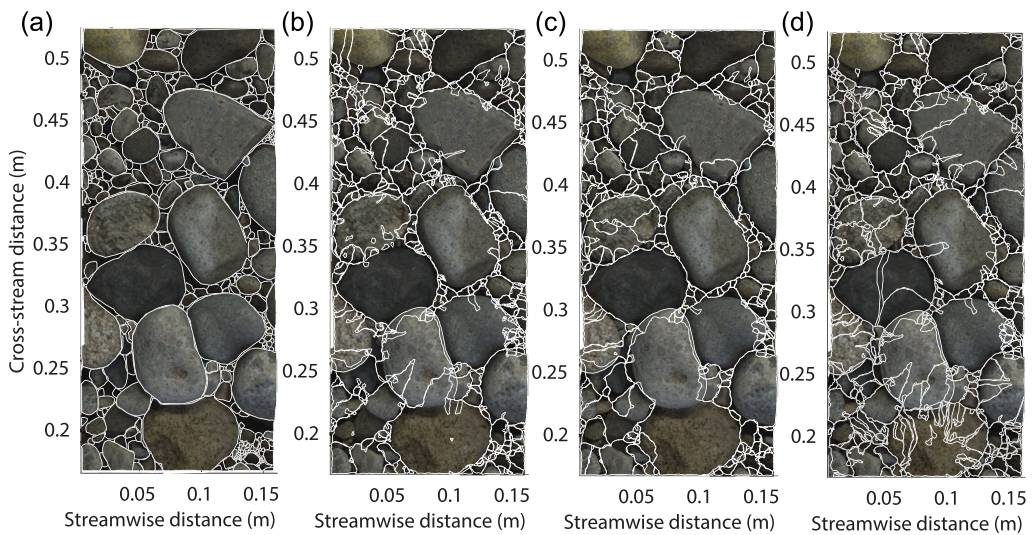


FIGURE 7 Orthomosaics of bed areas used in G3Point/Pro+ validation for the wide GSD (grain size distribution) experiments. Bed areas are the same as those in the white boxes in Figure 1. White lines show (a) manual grain perimeters and (b, c) perimeters from the optimal G3Point input variable combination (see Table 1) with a k value of (b) 10 and (c) 15. (d) Perimeters from a G3Point input variable combination ($n_{\min} = 50$, $C_F = 0.2$, $\alpha = 60^\circ$, $\beta = 10^\circ$, $\phi_{\text{flat}} = 0.1$) that produced reasonably accurate G3Point/Pro+ grain size, protrusion and τ_c distributions.

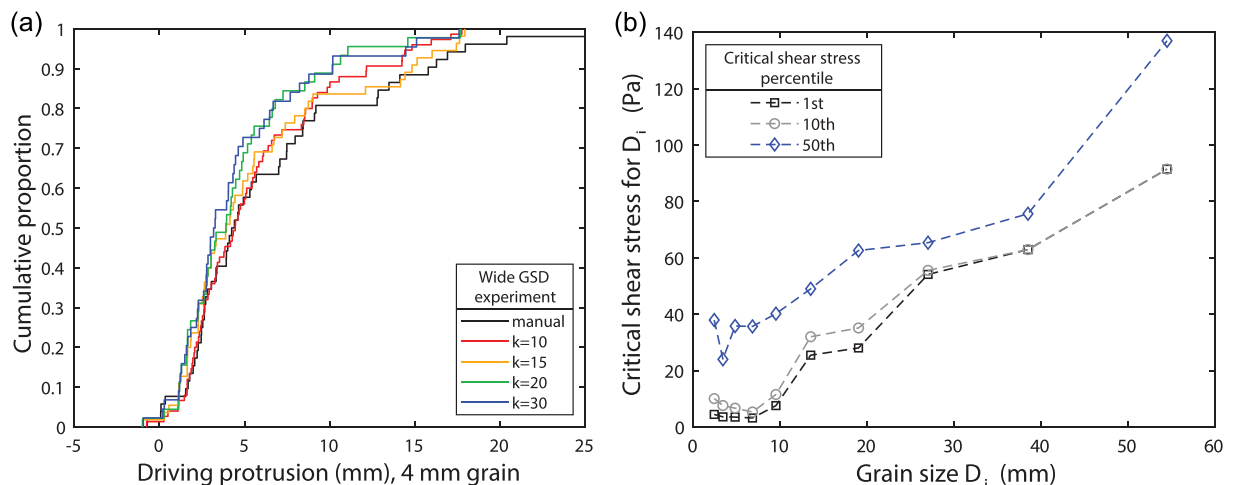


FIGURE 8 Example using G3Point/Pro+ to obtain protrusion and τ_{ci} for each grain size bin. (a) Manual-based (black line) and G3Point/Pro+ (coloured lines labelled with k values) driving protrusion distributions for the 4-mm grain size bin in the wide GSD (grain size distribution) experiment. (b) Example G3Point/Pro+ calculated (with $k = 10$) τ_{ci} distribution percentiles (1st, 10th and 50th) for each grain size bin in the wide GSD experiment. The optimal G3Point input variables for the wide GSD experiment (see Table 1) were used in all calculations.

4.2 | Potential Pro+ calculations for each grain size

The protrusion and τ_c distributions for the entire bed in Figure 5 obscure that each grain size bin has unique distributions of these variables. We cannot assess the accuracy of G3Point/Pro+ protrusion and τ_c distributions for each grain size bin because we used small bed areas in our manual measurements, which resulted in a low number of sampled grains in each bin. As an example application of G3Point/Pro+, we show the p_D distribution in the wide GSD experiment for one grain size bin (4 mm) that potentially had enough manually sampled particles (51) to define a distribution. The optimised G3Point input variable combination for this experiment (Table 1) also provided a G3Point/Pro+ p_D distribution that generally matched the manual-

based distribution for the 4-mm grain size bin (Figure 8a). Calibrated G3Point inputs to Pro+ may also allow for accurate G3Point/Pro+ protrusion estimates for a given grain size (D_i) of interest.

With a greater number of particles and therefore protrusion measurements in each grain size bin, Pro+ can similarly estimate the τ_{ci} distribution for each D_i , which are used in hiding functions. Although we lack the proper sample size to develop hiding functions, we tested if τ_{ci} increases with D_i , which is commonly expected unless hiding effects perfectly balance grain weight effects to produce equal mobility onset of motion conditions. We used low example percentiles (1st, 10th and 50th) of the τ_{ci} distributions to represent particles that are easily mobile. These τ_{ci} percentiles generally increased with larger D_i (Figure 8b), suggesting Pro+ could create hiding functions after further testing.

4.3 | Pro+ applicability and input considerations

Several limitations need to be considered before applying Pro+ to a wide range of river systems. Obtaining the representative bed point cloud or DEM (converted to a point cloud format) is the key to accurate Pro+ estimates. The representative bed area to sample (e.g. 1×1 m) depends on (1) whether only τ_{c50}^* or τ_{ci}^* for all grain sizes is needed, (2) the area needed to obtain a representative grain size sample, and (3) the area needed to accurately determine k_s and protrusion, which are functions of either the D_{84} or σ_z . We hypothesise that G3Point/deep learning/Pro+ estimated D_{50} and τ_{c50}^* could require a sample size of grains similar to that used for pebble counts. If τ_{ci}^* for all grain sizes is desired, then a larger sample size and therefore bed area is required to ensure proper sampling in all grain size bins. The distance over which protrusion and k_s must be measured is still an open research area, although our results and those of Smith et al. (2023) suggest that protrusion may be relatively insensitive to search distance. If bedform roughness is present, care must be taken in detrending bed elevations and in the distance over which k_s is measured to properly include the effects of bedforms on flow roughness (see details in Bertin et al., 2017; Powell et al., 2016).

The streambed point cloud could be obtained through photographs coupled with SfM photogrammetry, ground-based LiDAR, or possibly the new iPhone LiDAR if resolution improves (Monsalve et al., 2023). All of these methods generally require an unsubmerged bed and/or submersible cameras to eliminate potential water distortion and reflection effects. Calculations to remove these water effects (Partama et al., 2018; Zhang et al., 2022) may also allow for Pro+ application on submerged beds. For coupled G3Point/Pro+ application to gravel-bedded rivers, G3Point needs calibration with some measured GSD for Pro+ to provide generally accurate protrusion and τ_c distributions. If the point cloud for G3Point/Pro+ is from photographs and SfM, the calibrating GSD could be manually measured on a scaled orthomosaic as performed here. This would eliminate some of the uncertainties in G3Point calibration that arise from different GSD sampling methods (Steer et al., 2022).

Although we tested G3Point and Pro+ using grain sizes as small as 2 mm, G3Point cannot provide accurate GSD for beds with a large proportion of sand (see discussion in Steer et al., 2022). Sand content also influences τ_c^* for gravel (Wilcock & Crowe, 2003) by potentially altering k_s (Venditti et al., 2010), ϕ_p or ϕ_f , but the variation of these three Pro+ inputs with bed sand content is uncertain. Given these uncertainties, we do not recommend using Pro+ on beds with significant surface sand contents.

In addition to grain size considerations, Pro+ also requires numerous input variables for protrusion and τ_c^* calculations, which are discussed in detail in Section 2 and the supporting information. In particular, the mean and standard deviation of ϕ_f can strongly influence calculated resisting forces and τ_c^* values (Yager, Schmeeckle, & Badoux, 2018). These ϕ_f values can be informed by those in Yager, Schmeeckle and Badoux (2018) or by resisting force measurements using a load cell in the same bed area after topographic data collection. The input mean and standard deviation of ϕ_f can be adjusted until the load cell and output Pro+ resisting force distributions match. Future studies could develop correlations between measured resisting forces and bed structural components estimated from point clouds such as imbrication, interlocking and clustering (Aberle &

Nikora, 2006; Curran & Waters, 2014; Hodge et al., 2009; Mao, 2012; Ockelford & Haynes, 2013; Wu et al., 2018). Such correlations could then be included in Pro+ to estimate ϕ_f values only from point clouds.

4.4 | Application of Pro+ to predict and understand τ_c^*

Pro+ can provide informed estimates of τ_{c50}^* and hiding function exponents in many gravel-bedded rivers using the actual bed conditions (i.e. protrusion, grain size and roughness) and some of the mechanics (e.g. applied and resisting forces) of sediment motion. These Pro+ estimates could replace the often arbitrary and subjective choices of τ_{c50}^* and hiding function exponents from the wide range of values in the literature (Buffington & Montgomery, 1997). We expect that such informed estimates of τ_{c50}^* would improve sediment transport, channel stability and onset of motion predictions.

In addition to potentially supplying a single representative τ_{ci}^* value, Pro+ also provides a distribution of τ_{ci}^* for a given grain size because of different particle arrangements and local flow conditions. In calculations of bedload transport, shear stress distributions are usually ignored in favour of single values of τ_{ci}^* and reach-averaged applied shear stresses. The use of applied shear stress distributions and τ_{ci}^* distributions in bedload transport equations can reduce errors in predicted sediment fluxes compared to using single values of these shear stresses (Ferguson, 2003; Monsalve et al., 2016; Segura & Pitlick, 2015; Yager & Schmeeckle, 2013; Yager, Venditti, et al., 2018). When possible, we recommend using the entire Pro+ τ_{ci}^* distribution that could be coupled with reach-scale or patch-scale shear stress distributions from 2D hydraulic models following the methods outlined in Monsalve et al. (2016) and Segura and Pitlick (2015).

Pro+ could also be used to mechanistically explain some of the observed τ_{c50}^* variability between rivers. Protrusion is a dominant control on driving forces, resisting forces and τ_c^* (Hodge et al., 2020; Kirchner et al., 1990; Schmeeckle et al., 2007; Smith et al., 2023; Xie et al., 2023; Yager, Schmeeckle, & Badoux, 2018), and Pro+ explicitly includes these effects. Similarly, Pro+ could be used to explain the large measured variability in hiding function exponents, which are likely partly controlled by bed GSD (Shvidchenko et al., 2001) and protrusion. Finally, Pro+ could estimate temporal changes in τ_c^* given the potential influence of protrusion on τ_c^* variations with time (Masteller & Finnegan, 2017).

5 | CONCLUSIONS

Critical Shields stresses for the onset of sediment transport have considerable uncertainty but can have large impacts on channel stability and sediment transport calculations. To address this problem, we developed a mechanistic-based method called Pro+ that builds upon existing software that calculates grain sizes from bed point clouds. When coupled with grain size estimating software, Pro+ can determine particle protrusion and τ_c^* distributions as well as hiding functions in gravel-bedded rivers. Care must be taken that the grain estimating software correctly identifies grain boundaries and grain locations, which were a large potential source of error in protrusion and τ_c^* calculations. Pro+ obtained τ_c^* distributions can provide

informed estimates of the onset of motion rather than an arbitrarily chosen τ_c^* value from the wide range of scatter observed in gravel-bedded rivers.

AUTHOR CONTRIBUTIONS

E.M. Yager contributed to the paper through obtaining the funding, conceptualisation, code development, data analysis and writing. J. Shim contributed to data collection; R. A. Hodge contributed to conceptualisation and writing; D. Tonina contributed to obtaining funding and writing; J. P. L. Johnson contributed to conceptualisation and writing; A. Monsalve contributed to obtaining funding, conceptualisation, and writing; and L. Telfer contributed to writing and data analysis.

ACKNOWLEDGEMENTS

Funding for this project was provided a National Science Foundation grant EAR1921790 to E.M. Yager. We thank Gravel Bed Rivers 9 participants for helpful discussion of these results during the meeting, and two anonymous reviewers and AE Luca Mao for providing comments on an earlier version of this manuscript.

DATA AVAILABILITY STATEMENT

The Pro+ code, user manual and example data to run the code are available at <https://github.com/eyager/ProPlus>.

ORCID

Elowyn M. Yager  <https://orcid.org/0000-0002-3382-2356>

Rebecca Hodge  <https://orcid.org/0000-0002-8792-8949>

Daniele Tonina  <https://orcid.org/0000-0002-1866-1013>

REFERENCES

Aberle, J. & Nikora, V. (2006) Statistical properties of armored gravel bed surfaces. *Water Resources Research*, 42(11), W11414. Available from: <https://doi.org/10.1029/2005WR004674>

Aberle, J. & Smart, G.M. (2003) The influence of roughness structure on flow resistance on steep slopes. *Journal of Hydraulic Research*, 41(3), 259–269. Available from: <https://doi.org/10.1080/00221680309499971>

Bathurst, J.C. (2013) Critical conditions for particle motion in coarse bed materials of nonuniform size distribution. *Geomorphology*, 197, 170–184. Available from: <https://doi.org/10.1016/j.geomorph.2013.05.008>

Bertin, S., Groom, J. & Friedrich, H. (2017) Isolating roughness scales of gravel-bed patches. *Water Resources Research*, 53(8), 6841–6856. Available from: <https://doi.org/10.1002/2016WR020205>

Bi, D., Zhang, J., Chakraborty, B. & Behringer, R.P. (2011) Jamming by shear. *Nature*, 480(7377), 355–358. Available from: <https://doi.org/10.1038/nature10667>

Budwig, R. & Goodwin, P. (2012) Ecohydraulics Research Mountain StreamLab—A facility for collaborative research and education. In: Aung, W., Ilic, V., Mertanen, O., Moscinski, J. & Uhomoibh, J. (Eds.) *Innovations 2012: world innovations in engineering education and research*, iNEER, Potomac, MD, pp. 17–28.

Buffington, J.M., Dietrich, W.E. & Kirchner, J.W. (1992) Friction angle measurements on a naturally formed gravel streambed: implications for critical boundary shear stress. *Water Resources Research*, 28(2), 411–425. Available from: <https://doi.org/10.1029/91WR02529>

Buffington, J.M. & Montgomery, D.R. (1997) A systematic analysis of eight decades of incipient motion studies, with special reference to gravel-bedded rivers. *Water Resources Research*, 33(8), 1993–2029. Available from: <https://doi.org/10.1029/96WR03190>

Buscombe, D. & Masselink, G. (2009) Grain-size information from the statistical properties of digital images of sediment. *Sedimentology*, 56(2), 421–438. Available from: <https://doi.org/10.1111/j.1365-3091.2008.00977.x>

Buscombe, D., Rubin, D.M. & Warrick, J.A. (2010) A universal approximation of grain size from images of noncohesive sediment. *Journal of Geophysical Research - Earth Surface*, 115(F2), F02015. Available from: <https://doi.org/10.1029/2009JF001477>

Butler, J.B., Lane, S.N. & Chandler, J.H. (2001) Automated extraction of grain-size data from gravel surfaces using digital image processing. *Journal of Hydraulic Research*, 39(5), 519–529. Available from: <https://doi.org/10.1080/00221686.2001.9628276>

Buxton, T.H., Buffington, J.M., Yager, E.M., Hassan, M.A. & Fremier, A.K. (2015) The relative stability of salmon redds and unspawned streambeds. *Water Resources Research*, 6074–6092(8), 6074–6092. Available from: <https://doi.org/10.1002/2015WR016908>

Charru, F., Mouilleron, H. & Eiff, O. (2004) Erosion and deposition of particles on a bed sheared by a viscous flow. *Journal of Fluid Mechanics*, 519, 55–80. Available from: <https://doi.org/10.1017/S0022112004001028>

Chen, Z., Scott, T.R., Bearman, S., Anand, H., Keating, D., Scott, C., et al. (2020) Geomorphological analysis using unpiloted aircraft systems, structure from motion, and deep learning. In: *Presented at the 2020 IEEE/RSJ international conference on intelligent robots and systems (IROS)*, Las Vegas, NV, USA, IEEE, pp. 1276–1283. 24 October [online]. Available from: <https://ieeexplore.ieee.org/document/9341354/>

Cúñez, F.D., Franklin, E.M., Houssais, M., Arratia, P. & Jerolmack, D.J. (2022) Strain hardening by sediment transport. *Physical Review Research*, 4(2), L022055. Available from: <https://doi.org/10.1103/PhysRevResearch.4.L022055>

Curran, J.C. & Tan, L. (2014) The effect of cluster morphology on the turbulent flows over an armored gravel bed surface. *Journal of Hydro-Environment Research*, 8(2), 129–142. Available from: <https://doi.org/10.1016/j.jher.2013.11.002>

Curran, J.C. & Waters, K.A. (2014) The importance of bed sediment sand content for the structure of a static armor layer in a gravel bed river. *Journal of Geophysical Research - Earth Surface*, 119(7), 1484–1497. Available from: <https://doi.org/10.1002/2014JF003143>

Daniels, K.E., Kollmer, J.E. & Puckett, J.G. (2017) Photoelastic force measurements in granular materials. *Review of Scientific Instruments*, 88(5), 051808. Available from: <https://doi.org/10.1063/1.4983049>

Duffin, J., Yager, E.M., Buffington, J.M., Benjankar, R., Borden, C. & Tonina, D. (2023) Impact of flow regulation on stream morphology and habitat quality distribution. *Science of the Total Environment*, 878, 163016. Available from: <https://doi.org/10.1016/j.scitotenv.2023.163016>

Fenton, J.D. & Abbott, J.E. (1977) Initial movement of grains on a stream bed: the effect of relative protrusion. *Proceedings of the Royal Society a: Mathematical, Physical and Engineering Sciences*, 352(1671), 523–537. Available from: <https://doi.org/10.1098/rspa.1977.0014>

Ferguson, R. (2003) The missing dimension: effects of lateral variation on 1-D calculations of fluvial bedload transport. *Geomorphology*, 56(1-2), 1–14. Available from: [https://doi.org/10.1016/S0169-555X\(03\)00042-4](https://doi.org/10.1016/S0169-555X(03)00042-4)

Ferguson, R.I., Hardy, R.J. & Hodge, R.A. (2019) Flow resistance and hydraulic geometry in bedrock rivers with multiple roughness length scales. *Earth Surface Processes and Landforms*, 44(12), 2437–2449. Available from: <https://doi.org/10.1002/esp.4673>

Garcia, M. (Ed.) (2008) *Sedimentation engineering: processes, measurements, modeling, and practice*, 110th edition. Reston, VA [online]. Available from: 10.1061/9780784408148: American Society of Civil Engineers.

Garefalakis, P., Do Prado, A.H., Mair, D., Douillet, G.A., Nyffenegger, F. & Schlunegger, F. (2023) Comparison of three grain size measuring methods applied to coarse-grained gravel deposits. *Sedimentary Geology*, 446, 106340. Available from: <https://doi.org/10.1016/j.sedgeo.2023.106340>

Graham, D.J. (2005) A transferable method for the automated grain sizing of river gravels. *Water Resources Research*, 41(7), W07020. Available from: <https://doi.org/10.1029/2004WR003868>

Haynes, H. & Pender, G. (2007) Stress history effects on graded bed stability. *Journal of Hydraulic Engineering*, 133(4), 343–349. Available from: [https://doi.org/10.1061/\(ASCE\)0733-9429\(2007\)133:4\(343\)](https://doi.org/10.1061/(ASCE)0733-9429(2007)133:4(343))

Heald, J., McEwan, I. & Tait, S. (2004) Sediment transport over a flat bed in a unidirectional flow: simulations and validation. *Philosophical transactions of the Royal Society of London. Series a: mathematical, physical and engineering sciences*, 362, pp. 1973–1986.

Hodge, R., Brasington, J. & Richards, K. (2009) Analysing laser-scanned digital terrain models of gravel bed surfaces: linking morphology to sediment transport processes and hydraulics. *Sedimentology*, 56(7), 2024–2043. Available from: <https://doi.org/10.1111/j.1365-3091.2009.01068.x>

Hodge, R.A. & Buechel, M.E.H. (2022) The influence of bedrock river morphology and alluvial cover on gravel entrainment. Part 2: modelling critical shear stress. *Earth Surface Processes and Landforms*, 47(14), 3348–3360. Available from: <https://doi.org/10.1002/esp.5462>

Hodge, R.A., Sear, D.A. & Leyland, J. (2013) Spatial variations in surface sediment structure in riffle-pool sequences: a preliminary test of the differential sediment entrainment hypothesis (DSEH). *Earth Surface Processes and Landforms*, 38(5), 449–465. Available from: <https://doi.org/10.1002/esp.3290>

Hodge, R.A., Voepel, H., Leyland, J., Sear, D.A. & Ahmed, S. (2020) X-ray computed tomography reveals that grain protrusion controls critical shear stress for entrainment of fluvial gravels. *Geology*, 48(2), 149–153. Available from: <https://doi.org/10.1130/G46883.1>

Hodge, R.A., Voepel, H., Yager, E.M., Leyland, J., Johnson, J.P.L., Sear, D.A., et al. In review. Improving predictions of critical shear stress in gravel bed rivers: identifying the onset of sediment transport and quantifying sediment structure. *Earth Surface Processes and Landforms*.

Johnson, J.P.L. (2014) A surface roughness model for predicting alluvial cover and bed load transport rate in bedrock channels: bedrock roughness alluvial cover model. *Journal of Geophysical Research - Earth Surface*, 119(10), 2147–2173. Available from: <https://doi.org/10.1002/2013JF003000>

Johnson, J.P.L. (2016) Gravel threshold of motion: a state function of sediment transport disequilibrium? *Earth Surface Dynamics*, 4(3), 685–703. Available from: <https://doi.org/10.5194/esurf-4-685-2016>

Johnson, J.P.L. (2017) Clustering statistics, roughness feedbacks, and randomness in experimental step-pool morphodynamics. *Geophysical Research Letters*, 44(8), 3653–3662. Available from: <https://doi.org/10.1002/2016GL072246>

Kirchner, J.W., Dietrich, W.E., Iseya, F. & Ikeda, H. (1990) The variability of critical shear stress, friction angle, and grain protrusion in water-worked sediments. *Sedimentology*, 37(4), 647–672. Available from: <https://doi.org/10.1111/j.1365-3091.1990.tb00627.x>

Lacey, R.W.J. & Roy, A.G. (2007) A comparative study of the turbulent flow field with and without a pebble cluster in a gravel bed river. *Water Resources Research*, 43, W05502, Available from: <https://doi.org/10.1029/2006WR005027>

Lamb, M.P., Brun, F. & Fuller, B.M. (2017a) Direct measurements of lift and drag on shallowly submerged cobbles in steep streams: implications for flow resistance and sediment transport. *Water Resources Research*, 53(9), 7607–7629. Available from: <https://doi.org/10.1002/2017WR020883>

Lamb, M.P., Brun, F. & Fuller, B.M. (2017b) Hydrodynamics of steep streams with planar coarse-grained beds: turbulence, flow resistance, and implications for sediment transport. *Water Resources Research*, 53(3), 2240–2263. Available from: <https://doi.org/10.1002/2016WR019579>

Lamb, M.P., Dietrich, W.E. & Venditti, J.G. (2008) Is the critical Shields stress for incipient sediment motion dependent on channel-bed slope? *Journal of Geophysical Research*, 113(F2), F02008. Available from: <https://doi.org/10.1029/2007JF000831> [online].

Luo, M., Jiang, Y., Wang, S., Liu, X. & Huang, E. (2023) The effect of stress history on fluctuation of bedload transport rate and bed topography in gravel-bed streams. *Journal of Hydrology*, 616, 128732. Available from: <https://doi.org/10.1016/j.jhydrol.2022.128732>

Mao, L. (2012) The effect of hydrographs on bed load transport and bed sediment spatial arrangement. *Journal of Geophysical Research*, 117(F3), F03024. Available from: <https://doi.org/10.1029/2012JF002428>

Masteller, C.C. & Finnegan, N.J. (2017) Interplay between grain protrusion and sediment entrainment in an experimental flume. *Journal of Geophysical Research - Earth Surface*, 122(1), 274–289. Available from: <https://doi.org/10.1002/2016JF003943>

Masteller, C.C., Finnegan, N.J., Turowski, J.M., Yager, E.M. & Rickenmann, D. (2019) History-dependent threshold for motion revealed by continuous bedload transport measurements in a Steep Mountain stream. *Geophysical Research Letters*, 46(5), 2583–2591. Available from: <https://doi.org/10.1029/2018GL081325>

Monsalve, A., Yager, E.M. & Schmeeckle, M.W. (2017) Effects of bed forms and large protruding grains on near-bed flow hydraulics in low relative submergence conditions. *Journal of Geophysical Research - Earth Surface*, 122, 1845–1866. Available from: <https://doi.org/10.1002/2016JF004152>

Monsalve, A., Yager, E.M. & Tonina, D. (2023) Evaluating Apple iPhone LiDAR measurements of topography and roughness elements in coarse bedded streams. *Journal of Ecohydraulics*, 1–11, 1–11. Available from: <https://doi.org/10.1080/24705357.2023.2204087>

Monsalve, A., Yager, E.M., Turowski, J.M. & Rickenmann, D. (2016) A probabilistic formulation of bed load transport to include spatial variability of flow and surface grain size distributions. *Water Resources Research*, 52(5), 3579–3598. Available from: <https://doi.org/10.1002/2015WR017694>

Ockelford, A., Woodcock, S. & Haynes, H. (2019) The impact of inter-flood duration on non-cohesive sediment bed stability. *Earth Surface Processes and Landforms*, 44(14), 2861–2871. Available from: <https://doi.org/10.1002/esp.4713>

Ockelford, A.-M. & Haynes, H. (2013) The impact of stress history on bed structure. *Earth Surface Processes and Landforms*, 38(7), 717–727. Available from: <https://doi.org/10.1002/esp.3348>

Partama, I.G.Y., Kanno, A., Ueda, M., Akamatsu, Y., Inui, R., Sekine, M., et al. (2018) Removal of water-surface reflection effects with a temporal minimum filter for UAV-based shallow-water photogrammetry: removal of water-surface reflection effects for UAV-photogrammetry. *Earth Surface Processes and Landforms*, 43(12), 2673–2682. Available from: <https://doi.org/10.1002/esp.4399>

Powell, D.M., Ockelford, A., Rice, S.P., Hillier, J.K., Nguyen, T., Reid, I., et al. (2016) Structural properties of Mobile armors formed at different flow strengths in gravel-bed rivers: mobile armor structure. *Journal of Geophysical Research - Earth Surface*, 121(8), 1494–1515. Available from: <https://doi.org/10.1002/2015JF003794>

Pretzlaw, K.L.G., Johnson, J.P.L. & Bradley, D.N. (2020) Smartrock transport in a mountain stream: bedload hysteresis and changing thresholds of motion. *Water Resources Research*, 56(11), e2020WR028150. Available from: <https://doi.org/10.1029/2020WR028150>

Recking, A. (2009) Theoretical development on the effects of changing flow hydraulics on incipient bed load motion. *Water Resources Research*, 45(4), W04401. Available from: <https://doi.org/10.1029/2008WR006826>

Rickenmann, D. (2020) Effect of sediment supply on cyclic fluctuations of the disequilibrium ratio and threshold transport discharge, inferred from bedload transport measurements over 27 years at the Swiss Erlenbach stream. *Water Resources Research*, 56(11), e2020WR027741. Available from: <https://doi.org/10.1029/2020WR027741>

Sanguinito, S. & Johnson, J. (2012) Quantifying gravel overlap and dislodgement forces on natural river bars: implications for particle entrainment. *Earth Surface Processes and Landforms*, 37(1), 134–141. Available from: <https://doi.org/10.1002/esp.2237>

Schmeeckle, M.W., Nelson, J.M. & Shreve, R.L. (2007) Forces on stationary particles in near-bed turbulent flows. *Journal of Geophysical Research*, 112(F2), F02003. Available from: <https://doi.org/10.1029/2006JF000536>

Schmeeckle, M.W. & Nelson, J.M. (2003) Direct numerical simulation of bedload transport using a local, dynamic boundary condition. *Sedimentology*, 50(2), 279–301. Available from: <https://doi.org/10.1046/j.1365-3091.2003.00555.x>

Schneider, J.M., Rickenmann, D., Turowski, J.M. & Kirchner, J.W. (2015) Self-adjustment of stream bed roughness and flow velocity in a steep mountain channel. *Water Resources Research*, 51(10), 7838–7859. Available from: <https://doi.org/10.1002/2015WR016934>

Segura, C. & Pitlick, J. (2015) Coupling fluvial-hydraulic models to predict gravel transport in spatially variable flows. *Journal of Geophysical Research - Earth Surface*, 120(5), 834–855. Available from: <https://doi.org/10.1002/2014JF003302>

Shields, I.A. (1936) *Anwendung der Ähnlichkeitstheorie und der Turbulenzforschung auf die geschiebebewegung*. Preussischen Versuchsanstalt für Wasserbau, Berlin, Germany.

Shvidchenko, A.B., Pender, G. & Hoey, T.B. (2001) Critical shear stress for incipient motion of sand/gravel streambeds. *Water Resources Research*, 37(8), 2273–2283. Available from: <https://doi.org/10.1029/2000WR000036>

Smart, G.M., Duncan, M.J. & Walsh, J.M. (2002) Relatively rough flow resistance equations. *Journal of Hydraulic Engineering*, 128(6), 568–578. Available from: [https://doi.org/10.1061/\(ASCE\)0733-9429\(2002\)128:6\(568\)](https://doi.org/10.1061/(ASCE)0733-9429(2002)128:6(568))

Smith, H.E.J., Monsalve, A.D., Turowski, J.M., Rickenmann, D. & Yager, E.M. (2023) Controls of local grain size distribution, bed structure, and flow conditions on sediment mobility. *Earth Surface Processes and Landforms*, 48(10), esp.5599–esp.2004. Available from: <https://doi.org/10.1002/esp.5599>

Steer, P., Guerit, L., Lague, D., Crave, A. & Gourdon, A. (2022) Size, shape and orientation matter: fast and automatic measurement of grain geometries from 3D point clouds. *Esurf*, 10, 1211–1232. Available from: <https://egusphere.copernicus.org/preprints/2022/egusphere-2022-75/>.

Strom, K.B. & Papanicolaou, A.N. (2007) ADV measurements around a cluster microform in a Shallow Mountain stream. *Journal of Hydraulic Engineering*, 133(12), 1379–1389. Available from: [https://doi.org/10.1061/\(ASCE\)0733-9429\(2007\)133:12\(1379\)](https://doi.org/10.1061/(ASCE)0733-9429(2007)133:12(1379))

Turowski, J.M., Badoux, A. & Rickenmann, D. (2011) Start and end of bedload transport in gravel-bed streams. *Geophysical Research Letters*, 38(4), L04401. Available from: <https://doi.org/10.1029/2010GL046558>

Venditti, J.G., Dietrich, W.E., Nelson, P.A., Wydzga, M.A., Fadde, J. & Sklar, L. (2010) Effect of sediment pulse grain size on sediment transport rates and bed mobility in gravel bed rivers. *Journal of Geophysical Research*, 115(F3), F03039. Available from: <https://doi.org/10.1029/2009JF001418>

Voepel, H., Leyland, J., Hodge, R.A., Ahmed, S. & Sear, D. (2019) Development of a vector-based 3D grain entrainment model with application to X-ray computed tomography scanned riverbed sediment. *Earth Surface Processes and Landforms*, 44(15), 3057–3077. Available from: <https://doi.org/10.1002/esp.4608>

Walicka, A., Pfeifer, N., Borkowski, A. & Józków, G. (2021) An automatic method for the measurement of coarse particle movement in a mountain riverbed. *Measurement*, 174, 109029. Available from: <https://doi.org/10.1016/j.measurement.2021.109029>

Wiberg, P.L. & Smith, J.D. (1987) Calculations of the critical shear stress for motion of uniform and heterogeneous sediments. *Water Resources Research*, 23(8), 1471–1480. Available from: <https://doi.org/10.1029/WR023i008p01471>

Wilcock, P.R. (1993) Critical shear stress of natural sediments. *Journal of Hydraulic Engineering*, 119(4), 491–505. Available from: [https://doi.org/10.1061/\(ASCE\)0733-9429\(1993\)119:4\(491\)](https://doi.org/10.1061/(ASCE)0733-9429(1993)119:4(491))

Wilcock, P.R. & Crowe, J.C. (2003) Surface-based transport model for mixed-size sediment. *Journal of Hydraulic Engineering*, 129(2), 120–128. Available from: [https://doi.org/10.1061/\(ASCE\)0733-9429\(2003\)129:2\(120\)](https://doi.org/10.1061/(ASCE)0733-9429(2003)129:2(120))

Wu, F.-C., Wang, C.-K. & Huang, G.-H. (2018) Delineation of gravel-bed clusters via factorial kriging. *Geomorphology*, 308, 161–174. Available from: <https://doi.org/10.1016/j.geomorph.2018.02.013>

Wu, F.-C., Wang, C.-K. & Lo, H.P. (2021) FKgrain: a topography-based software tool for grain segmentation and sizing using factorial kriging. *Earth Science Informatics*, 14(4), 2411–2421. Available from: <https://doi.org/10.1007/s12145-021-00660-z>

Xie, Y., Melville, B.W., Shamseldin, A.Y., Whittaker, C.N. & Yang, Y. (2023) Direct measurement of the inertial drag and lift forces on entrained coarse particles at various protrusion heights. *Earth Surface Processes and Landforms*, 48(2), 371–385. Available from: <https://doi.org/10.1002/esp.5491>

Yager, E.M., Dietrich, W.E., Kirchner, J.W. & McArdell, B.W. (2012) Prediction of sediment transport in step-pool channels. *Water Resources Research*, 48(1), W01541. Available from: <https://doi.org/10.1029/2011WR010829>

Yager, E.M., Schmeeckle, M.W. & Badoux, A. (2018) Resistance is not futile: grain resistance controls on observed critical Shields stress variations. *Journal of Geophysical Research - Earth Surface*, 123, 3308–3322. Available from: <https://doi.org/10.1029/2018JF004817>

Yager, E.M. & Schmeeckle, M.W. (2013) The influence of vegetation on turbulence and bed load transport. *Journal of Geophysical Research - Earth Surface*, 118(3), 1585–1601. Available from: <https://doi.org/10.1002/jgrf.20085>

Yager, E.M., Venditti, J.G., Smith, H.J. & Schmeeckle, M.W. (2018) The trouble with shear stress. *Geomorphology*, 323, 41–50. Available from: <https://doi.org/10.1016/j.geomorph.2018.09.008>

Yochum, S.E., Bledsoe, B.P., David, G.C.L. & Wohl, E. (2012) Velocity prediction in high-gradient channels. *Journal of Hydrology*, 424–425, 84–98. Available from: <https://doi.org/10.1016/j.jhydrol.2011.12.031>

Zhang, C., Sun, A., Hassan, M.A. & Qin, C. (2022) Assessing through-water structure-from-motion photogrammetry in gravel-bed rivers under controlled conditions. *Remote Sensing*, 14(21), 5351. Available from: <https://doi.org/10.3390/rs14215351>

SUPPORTING INFORMATION

Additional supporting information can be found online in the Supporting Information section at the end of this article.

How to cite this article: Yager, E.M., Shim, J., Hodge, R., Monsalve, A., Tonina, D., Johnson, J.P.L. et al. (2024) Pro+: Automated protrusion and critical shear stress estimates from 3D point clouds of gravel beds. *Earth Surface Processes and Landforms*, 1–16. Available from: <https://doi.org/10.1002/esp.5822>